ROM SAF Report 42
Ref: SAF/ROM/METO/REP/RSR/042
Web: www.romsaf.org
Date: 18 October 2021

EUMETSAT
ROM SAF
RADIO OCCULTATION METEOROLOGY

ROM SAF Report 42

A one-dimensional variational ionospheric retrieval for truncated GNSS Radio Occultation measurements

Sean Healy[1] and Ian Culverwell[2]

ECMWF[1] and Met Office, Exeter, UK[2]

Document Author Table

	Name	Function	Date
Prepared by:	S. Healy	ROM SAF Project Team	18 October 2021
Reviewed by:	A. VonEnglen	EUMETSAT	16 August 2021
Reviewed by:	-	-	-
Approved by:	K. B. Lauritsen	ROM SAF Project Manager	18 October 2021

Document Change Record

Issue/Revision	Date	By	Description
0.1	10 August 2021	S. Healy	First version for review
0.2	23 August 2021	S. Healy	Updates based on review
1.0	18 October 2021	S. Healy	Final Version

ROM SAF

The Radio Occultation Meteorology Satellite Application Facility (ROM SAF) is a decentralised processing centre under EUMETSAT which is responsible for operational processing of GRAS radio occultation (RO) data from the Metop and Metop-SG satellites and radio occultation data from other missions. The ROM SAF delivers bending angle, refractivity, temperature, pressure, humidity, and other geophysical variables in near real-time for NWP users, as well as reprocessed Climate Data Records (CDRs) and Interim Climate Data Records (ICDRs) for users requiring a higher degree of homogeneity of the RO data sets. The CDRs and ICDRs are further processed into globally gridded monthly-mean data for use in climate monitoring and climate science applications.

The ROM SAF also maintains the Radio Occultation Processing Package (ROPP) which contains software modules that aid users wishing to process, quality-control and assimilate radio occultation data from any radio occultation mission into NWP and other models.

The ROM SAF Leading Entity is the Danish Meteorological Institute (DMI), with Cooperating Entities: i) European Centre for Medium-Range Weather Forecasts (ECMWF) in Reading, United Kingdom, ii) Institut D'Estudis Espacials de Catalunya (IEEC) in Barcelona, Spain, and iii) Met Office in Exeter, United Kingdom. To get access to our products or to read more about the ROM SAF please go to: https://www.romsaf.org

Intellectual Property Rights

Abstract

A new one-dimensional variational (1D-Var) retrieval approach for ionospheric GNSS radio occultation (GNSS-RO) measurements is described. The approach maps a one-dimensional ionospheric electron density profile, modeled with multiple "VaryChap" layers, to bending angle space. It is demonstrated that gradient based minimisation techniques can be applied to this retrieval problem. The use of ionospheric bending angles is discussed. This approach potentially circumvents the need to for a Differential Code Bias (DCB) estimate when using the measurements. This new, general retrieval method is applicable to both standard GNSS-RO retrieval problems, and the truncated geometry of EUMETSAT's Metop Second Generation (Metop-SG), which will provide GNSS-RO measurements up to $\sim$ 500 km above the surface. It has been tested with 143 COSMIC measurements, and compared with other retrieval approaches. We find that the solution converges in 135 of the cases, but around 25 cases have high "cost at convergence" values. It is argued that 1D-Var diagnostics like cost at convergence would be useful for quality control (QC) in an operational system. In general, a two layer VaryChap solution is better than one layer. The two layer retrieval problem is well-posed when bending angles in the interval from 120 km to 500 km are available. However, the bending angles up to 750 km improve the solution. The climatological *a priori* information used in the 1D-Var is effectively a starting point for the 1D-Var minimisation, rather than a constraint on the final solution. The use of bending angles here may be relevant for how Metop-SG and other GNSS-RO measurements are used in ionospheric data assimilation systems in the future.

An ionospheric 1D-Var retrieval will be included in ROPP-11, which is scheduled for release in early 2022. A more detailed statistical analysis of the performance of the 1D-Var retrieval is given by Elvidge (2021) in ROM SAF Visiting Scientist Report 39 (VS39).

Contents

1 Introduction

The radio occultation instrument on EUMETSAT's Metop Second Generation (Metop-SG) satellites will measure up to 500 km above the Earth's surface, and provide measurements for ionospheric and space weather applications. The retrieval of ionospheric profile information from GNSS radio occultation (GNSS-RO) is well established (e.g., Hajj and Romans, 1998; Schreiner *et al.* 1999), using an Abel transform inversion approach. However, the 500 km upper limit for the Metop-SG observations complicates the application of the Abel transform, and alternative ionospheric retrievals techniques have to be explored for this particular truncated geometry. Lyu *et al.* (2019) have presented two new approaches for this problem, but the more accurate approach, AVHIRO, is currently too slow for possible operational applications (this problem is being worked on). They also suggest that gradient based minimisation techniques are difficult to apply to this retrieval problem because of non-linearity. In this work, we present a new method based on a variational (or "optimal estimation") approach (Rodgers, 2000).

The one dimensional variational (1D-Var) retrieval approach is used extensively in neutral atmosphere GNSS-RO applications (Healy and Eyre, 2000; Palmer *et al.* 2000). It is a more flexible than the Abel transform inversion, as it does not rely on an idealised measurement geometry. Specifically, the truncated Metop-SG geometry can be accounted for in a straight forward manner as part of the forward problem, $H(\mathbf{x})$, which maps the electron density profile information, $\mathbf{x}$, to "observation space", $\mathbf{y}$. In this work, the observation space will be bending angles. With the exception of Hajj and Romans (1998), most GNSS-RO ionospheric retrievals are based on slant total electron content values (STEC), S, where the electron density, n_e, is integrated along the path, s, between the GNSS and LEO satellites, $S = \int_s n_e(s)ds$. However, STEC values derived from GNSS phase measurements are relative quantities. This is because there is an ambiguity in the total number of wave cycles along the path between the two satellites (e.g., Dryud *et al.* 2008). These STEC values can be "leveled" using the pseudo-range measurements for the same path, but this processing step introduces a differential code bias (DCB), that also requires estimation. We show how bending angles are related to the derivative of STEC, dS/da, where a is the impact parameter of the ray path. Clearly, this derivative removes the sensitivity to any constant offsets and simplifies the problem. We note that bending angles are now assimilated in most global numerical weather prediction (NWP) data assimilation systems without bias correction, and they are considered "anchor measurements" because they constrain the bias corrections applied to other measurements (e.g., Poli *et al.* 2010).

The purpose of this report is to outline the theoretical basis of the new ionospheric 1D-Var retrieval. Some comparisons against Abel transform solutions and the AVHIRO approach of Lyu *et al.* (2019) will be presented to highlight different aspects of the new retrieval, but a more detailed statistical analysis of the retrieval approach will be presented by Elvidge (2021) in ROM SAF Visiting Scientist Report 39 (Referred to as "VS39" hereafter). In section 2.1 we introduce the variational technique, and then we relate dS/da to bending angles in section 2.2. The forward model is described in section 2.3, and the results and discussion/conclusions in sections 3 and 4, respectively.

2 Method

2.1 Variational Retrieval

The aim of a one-dimensional variational (1D-Var) retrieval approach is to combine the *a priori* ionospheric information in the state vector, $\mathbf{x_b}$, with a vector of observations, $\mathbf{y}$, in a statistically optimal way (Rodgers 2000). This is now a standard approach in neutral atmosphere applications. It involves minimising a cost function of the form,

$$J(\mathbf{x}) = \frac{1}{2}(\mathbf{x}-\mathbf{x_b})^{\mathbf{T}}\mathbf{B^{-1}}(\mathbf{x}-\mathbf{x_b}) + \frac{1}{2}(\mathbf{y}-H(\mathbf{x}))^{\mathbf{T}}\mathbf{R^{-1}}(\mathbf{y}-H(\mathbf{x})) \tag{2.1}$$

with respect to $\mathbf{x}$, where $\mathbf{B}$ is the assumed background error covariance matrix, $\mathbf{R}$ is the observation error covariance matrix and H is the forward operator, mapping the ionospheric state information, $\mathbf{x}$, to observation space. In this case, H is mapping parameters that define the vertical electron density profile to bending angles as a function of impact parameter.

The retrieval solution, $\mathbf{x_a}$, is the state which minimises the cost function, and it should be consistent with both $\mathbf{x_b}$ and $\mathbf{y}$, to within their expected error statistics. In general, the *a priori*, $\mathbf{x_b}$, provides information that is not well constrained by the observations in "ill-posed" retrieval problems, but we show that this problem is "well-posed". This means that the bending angle profile provides useful information about all the ionospheric variables in the state vector $\mathbf{x}$, and the uncertainty in the estimate of $\mathbf{x}$ is significantly reduced as a result of making the measurement. In this context, a useful feature of the 1D-Var is that it provides an estimate of the theoretical solution error covariance matrix, $\mathbf{A}$, given $\mathbf{B}$ and $\mathbf{R}$,

$$\mathbf{A} = (\mathbf{B^{-1}} + \mathbf{H^T R^{-1} H})^{-1} \tag{2.2}$$

where $\mathbf{H}$ is a matrix of partial derivatives of the observation values with respect to the state vector elements. In well-posed problems the diagonal elements of the $\mathbf{A}$ matrix are significantly smaller than the corresponding diagonal elements of the $\mathbf{B}$ matrix ($A_{i,i} < B_{i,i}$).

The 1D-Var approach should be more robust to measurement noise than the Abel transform because it is a weighted least-sqaures approach; it will not over-fit the measurements if the assumed observation error statistics, $\mathbf{R}$, are a reasonable approximation of the actual observation error statistics. The retrieval also produces useful diagnostics on the quality of the solution. These include the number of iterations required to converge, and the cost at convergence, $J(\mathbf{x_a})$, which ideally should be half the size of the observation vector, $2J(\mathbf{x_a}) = m \pm \sqrt{2m}$ (e.g., Rodgers, 2000), if the assumed error statistics are well specified. In this work, we use a Marquardt-Levenberg approach to minimise the cost function (Press *et al.* 1992).

2.2 Slant TEC

The slant total electron content (STEC) is defined as the electron density, n_e, integrated along a ray path, s, between the satellites ($S = \int n_e ds$). The measured excess phase delays, ϕ_i, are related to the STEC, S, with $\phi_i = -k_4 S/f_i^2 + C$ (Schreiner *et al.* 1999), where $k_4 = 40.3\mathrm{m^3 s^{-2}}$, f_i is the frequency of the signal and C is a constant, because of the ambiguity in the number of wave cycles (e.g., Dryud *et al.* 2008).

Assuming spherical symmetry – meaning that the electron density is only a function of height ($n_e(r)$) – the STEC, S, along the straight line path between the GNSS and LEO satellites, at radius values r_G and r_L, respectively, can be written as (Eq. 12, Schreiner *et al.* 1999)

$$S = \left[\int_a^{r_L} + \int_a^{r_G}\right] \frac{r n_e(r)}{\sqrt{(r^2 - a^2)}} dr \tag{2.3}$$

using $ds = rdr/\sqrt{(r^2 - a^2)}$, where a is the impact parameter, and $n_e(r)$ is the electron density at radius r. This expression can be integrated by parts

$$S = n_e(r_L)\sqrt{(r_L^2 - a^2)} - \left[\int_a^{r_L} + \int_a^{r_G}\right] \sqrt{(r^2 - a^2)} \frac{dn_e(r)}{dr} dr \tag{2.4}$$

noting that we have assumed the electron density at the GNSS satellite is $n_e(r_G) = 0$. Differentiating this with respect to the impact parameter, a, gives

$$\frac{dS}{da} = -\frac{n_e(r_L)a}{\sqrt{(r_L^2 - a^2)}} + a\left[\int_a^{r_L} + \int_a^{r_G}\right] \frac{\frac{dn_e(r)}{dr}}{\sqrt{(r^2 - a^2)}} dr \tag{2.5}$$

The integral is proportional to an approximate form of 1D bending angle integral which is linear in $n_e(r)$. Specifically, for a signal with frequency f_i, the bending angle, $\alpha_i(a)$, is approximately,

$$\alpha_i(a) \simeq \frac{k_4 a}{f_i^2}\left[\int_a^{r_L} + \int_a^{r_G}\right] \frac{\frac{dn_e(r)}{dr}}{\sqrt{(r^2 - a^2)}} dr \tag{2.6}$$

For example, this form of the ionospheric bending angle integral is assumed in the standard ionospheric bending angle correction (Vorob'ev and Krasil'nikova, 1994; Eq. 29, Kursinski *et al.* 1997). It also is interesting to note that Eq. 2.5 is singular at r_L as noted in Lei *et al.* (2007). This singularity is necessary for the Abel inversion using STEC values (See Appendix B).

The gradient of the phase delay is $d\phi_i/da = -(k_4/f_i^2)dS_i/da$. Given measurements at two frequencies, (f_1, f_2), assuming straight line paths with the same impact parameter, a, we can write

$$\frac{d(\phi_1 - \phi_2)}{da} = -k_4\left(\frac{1}{f_1^2} - \frac{1}{f_2^2}\right)\frac{dS}{da} \tag{2.7}$$

$$\frac{d(\phi_1 - \phi_2)}{da} = k_4\left(\frac{f_1^2 - f_2^2}{f_1^2 f_2^2}\right)\left[a\left[\int_a^{r_L} + \int_a^{r_G}\right] \frac{\frac{dn_e(r)}{dr}}{\sqrt{(r^2 - a^2)}} dr - \frac{n_e(r_L)a}{\sqrt{(r_L^2 - a^2)}}\right] \tag{2.8}$$

There is an apparently fortuitous cancellation of errors relevant to this problem. In the processing of real measurements, bending angle values are derived from the Doppler shift values assuming the refractive index at the LEO satellite is $n(r_L) = 1$. For circular orbits, this assumption does not effect the impact parameter, a, (The proportionality between Doppler shift and impact parameter for circular orbits is also exploited in the Full Spectral Inversion (FSI) technique (Jensen *et al.* 2003).) but it introduces a frequency dependent negative bias, b_i, in the bending angles equal to (Schreiner *et al.* 1999)

$$b_i = -\frac{k_4}{f_i^2}\frac{n_e(r_L)a}{\sqrt{(r_L^2 - a^2)}} \tag{2.9}$$

which normally cancels out in the dual frequency ionospheric correction of the bending angles. This suggests that a forward model that computes Eq. 2.8 can be compared directly with the bending angles derived assuming $n(r_L) = 1$,

$$\frac{d(\phi_1 - \phi_2)}{da} \simeq \alpha_2(a) - \alpha_1(a). \tag{2.10}$$

Therefore, this ionospheric retrieval can use either bending angle differences, or the derivative of phase delay differences with respect to impact parameter.

2.3 Forward Model $H(\mathbf{x})$

The forward model, $H(\mathbf{x})$, maps ionospheric electron density information, $\mathbf{x}$, to observation space. We assume that the ionosphere can be modeled with a sum of one-dimensional "VaryChap" layers (Nsumei *et al.* 2012), where the electron density is only a function of radius ($n_e(r)$), and horizontal variations in the electron density are neglected. The forward model, $H(\mathbf{x})$, computes Eq. 2.8 for each VaryChap layer, and then sums the layer values to obtain the total signal.

Each VaryChap layer is defined by four parameters:

1. Peak electron density: n_m
2. Height of peak electron density: r_m
3. Scale height parameter: H_m
4. Gradient of scale height with height: k

The total number of elements in the state vector, $\mathbf{x}$, is four times the number of VaryChap layers used in the retrieval.

The electron density from a VaryChap layer can be written as (Nsumei *et al.* 2012),

$$n_e(r) = n_m \sqrt{\frac{H_m}{H(r)}} \exp\left(\frac{1}{2}(1-u(r)-\exp(-u(r)))\right) \tag{2.11}$$

where $u(r) = (r-r_m)/H_m$ and $H(r) = H_m$ when $r < r_m$. For $(r \geq r_m)$,

$$u(r) = \frac{1}{k}\ln\left(\frac{H(r)}{H_m}\right) \tag{2.12}$$

and

$$H(r) = H_m + k(r-r_m) \tag{2.13}$$

where we note that k is assumed to be a constant in the VaryChap ionospheric model. The sensitivity of the electron density profile to k is illustrated in Figure 2.1. The $k = 0$ curve corresponds to the Chapman profile, and all curves are identical below 300 km.

The electron density gradient, required in Eq. 2.8 for the computation of the bending angles or phase/STEC derivatives for $(r < r_m)$ is given by

$$\frac{dn_e(r)}{dr} = \frac{n_e(r)}{2H(r)}(\exp(-u(r))-1) \tag{2.14}$$

and for $(r \geq r_m)$

$$\frac{dn_e(r)}{dr} = \frac{n_e(r)}{2H(r)}(\exp(-u(r))-1-k) \tag{2.15}$$

and we note that the gradient is not continuous at $r = r_m$, but the electron density is continuous.

To compute integrals of the form

$$\left[\int_a^{r_L} + \int_a^{r_G}\right] \frac{\frac{dn_e(r)}{dr}}{\sqrt{(r^2-a^2)}} dr \tag{2.16}$$

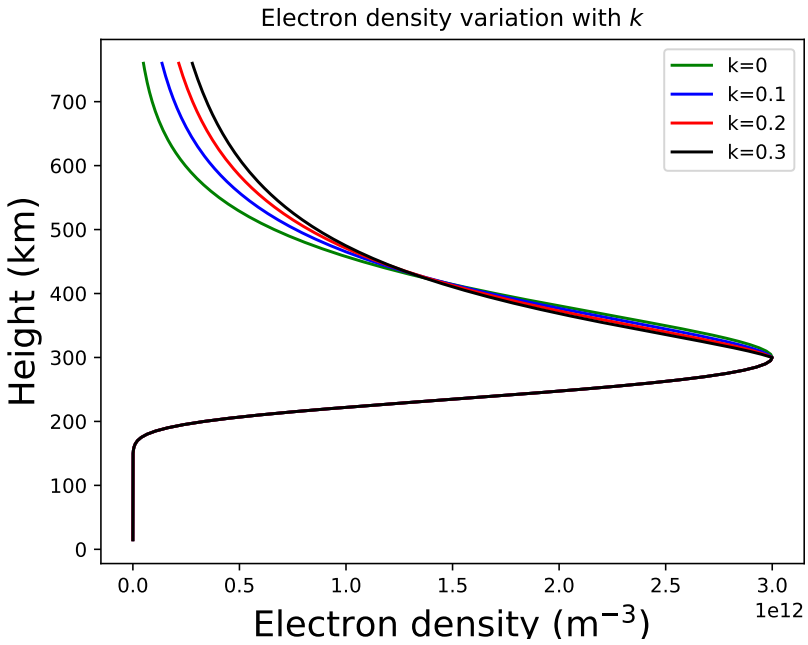

Figure 2.1: VaryChap electron density profiles given as a function of k in Eq. 2.13. The peak electron density n_m= 3 $\times 10^{12}$ m^{-3}, peaking at r_m=300 km and with H_m = 50 km.

in Eq. 2.8 we use the substitution $r = a\cosh(\theta)$, to remove the singularity at $r = a$. The integrals are computed numerically using Simpson's rule. A finer integration step, $\Delta\theta$, is used for the section of path below the LEO satellite, $r < r_L$.

The tangent linear of the forward model has also been developed for use in the Marquardt-Levenberg minimisation of the cost function (Press *et al.* 1992).

3 Results

The 1D-Var approach is being tested and validated against other retrievals in more detail in VS39 (Elvidge, 2021). In this work, we have tested the concept using 143 retrievals using data provided by IEEC, Barcelona, Spain. These are COSMIC measurements from "day of year" (DOY) 261 in 2011 (September 18). The files contain "geometry free" ($\phi_1 - \phi_2$) phase differences as function of impact parameter, a, up to the LEO satellite. The altitude of the COSMIC satellites is $\sim$ 800 km in these examples. The bending angles are computed with a finite difference approximation of $d(\phi_1 - \phi_2)/da$. The vertical separation between the bending angles is typically 500 m.

The retrieval code used in this work is the prototype science code, which formed the starting point in the official ROPP 11 ionospheric 1D-Var release. The code can be configured to use bending angles in a given vertical interval, and has a variable number of VaryChap layers. The variable vertical interval means we can investigate the impact of truncating the COSMIC data at 500 km.

We use a "climatological" VaryChap background, $\mathbf{x_b}$, which does not depend on either position or time. The VaryChap parameters are shown in Table 3.1. Results are presented for one and two VaryChap layers. In one layer retrievals, only the first four rows of Table 3.1 are used to populate $\mathbf{x_b}$. In practice, the lower layer is treated as a Chapman layer in the two calculations because the k value in row 8 of Table 3.1 are fixed to a small value. A fixed radius of curvature is used for all cases (6371 km) because the variable was not included in the test datasets.

The 1D-Var computation calculation stops if it has not converged in 45 iterations. The 1D-Var retrieval results are compared with the AVHIRO retrieval (Lyu *et al.* 2019), and an Abel transform solution. The Abel transform retrievals are not absolute electron density values, because we do not add the electron density at the LEO to the profile (See Appendix B). In addition, we have not corrected (calibrated) the bending angles to only include the section of the path below the LEO satellite, by subtracting positive elevation values with the same impact parameter (Section 3.1, Schreiner *et al*. 1999) However, the Abel solution should provide an indication of whether the 1D-Var results look reasonable. The implementation of the Abel transform assumes that the L2-L1 bending angle differences vary linearly in the vertical between observations. The Abel transform is then linear and the retrieved electron density profile can be computed as a matrix-vector product of the form $\mathbf{n_e} = \mathbf{A}\alpha$.

Table 3.1: The background state and uncertainty information used in the 1D-Var computations. The one layer computations just use the uppermost four rows. R_c is the radius of curvature.

Layer number	Variable(unit)	Value	Uncertainty (σ_b)
1	n_m (m^{-3})	1.0e12	5.0e11
1	$r_m - R_c$ (m)	3.0e5	1.5e5
1	H_m(m)	5.0e4	2.5e4
1	k (m/m)	0.015	0.075
2	n_m (m^{-3})	1.0e11	2.5e10
2	$r_m - R_c$ (m)	2.0e5	2.0e4
2	H_m (m)	2.0e4	1.0e4
2	k (m/m)	1.5e-5	7.5e-6

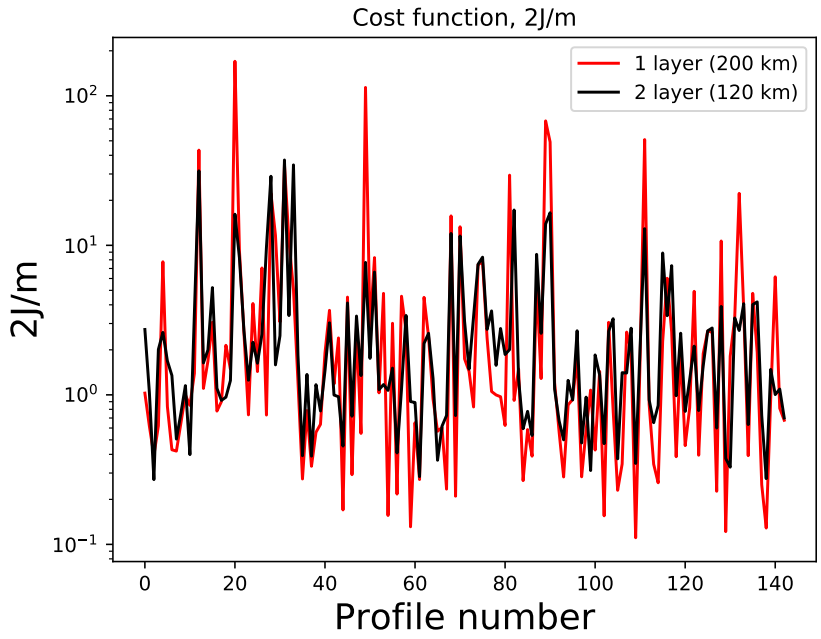

Figure 3.1: The cost at convergence values for the 1 layer (red line) and two layer (black line) retrievals.

We initially consider two retrieval configurations. The first is a single layer assimilating bending angles in the interval between 200 km to 500 km. The second is a two layer retrieval using data from 120 km up to 500 km. Note that extending a single layer down to 120 km does not work well. It produces higher cost function values, and appears to bias the peak electron density values low. We do not go below 120 km currently because the bending angle profiles contain vertical structure below 120 km which cannot be reproduced with either the 1 or 2 layer VaryChap retrievals. The standard deviation of the bending angle errors is assumed to be 2 microradians over the entire vertical range. The bending angle vertical error correlations are assumed to be zero, so the matrix $\mathbf{R}$ is diagonal. The 2 microradian noise level was essentially determined by trial and error, but it is comparable to the value used in neutral atmosphere applications in the middle/upper stratosphere. For example, ECMWF uses 3 microradians above $\sim$ 32 km when assimilating GNSS-RO data.

Figure 3.1 shows the 1D-Var cost function values at convergence divided by the number of observations ($2J/m$), and the Figure 3.2 is the number of iterations required for convergence. Ideally, if the background and observation error statistics are well specified, $2J/m \sim 1$ and large deviations from this are a useful quality control indicator. We use $2J/m > 5$ to indicate a poor quality retrieval. The one layer calculation tend to have larger outliers than the 2 layer calculations. There are 8 cases in both the 1 layer and 2 layer calculations which fail to converge in 45 iterations. Excluding these 8, the mean number of iterations required for convergence is 11.2 for the 1 layer case and 17.7 for the two layer retrieval. Of the 8 failures to converge, the number of $2J/m > 5$ was 7 and 5 for the 1 layer and 2 layer retrievals, respectively. More generally, the number of cases where $2J/m > 5$ was 25 and 21 for the 1 layer and 2 layer retrievals, respectively.

The performance of the 1D-Var is illustrated with 4 cases (See Appendix A) chosen because their retrieval diagnostics and convergence properties differ. In the first case ("case 1"), the 1D-Var retrievals converge to reasonable $2J/m$ values and these can be considered a good retrievals. In fact, this example is also shown in Figure 3 of Lyu *et al.* (2019). Figure 3.3 shows the bending angle profile of the observation (green line) and the 1D-Var solutions using 1 layer (blue) and two layers (red). The

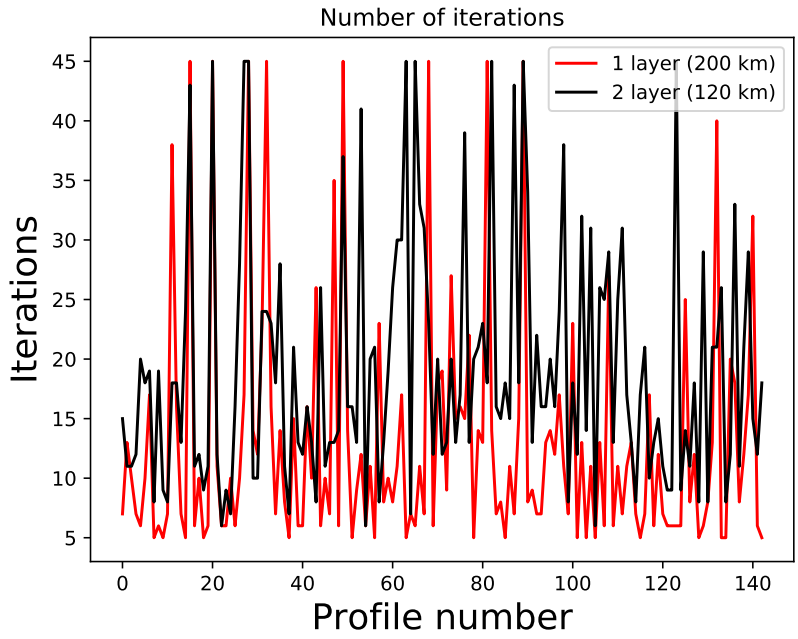

Figure 3.2: The number of 1D-Var iterations for the 1 layer (red line) and two layer (black line) retrievals. The retrieval exits at 45 iterations.

observed bending angle profile is noisier than the smooth profiles provided by the 1D-Var solutions. The simulated bending angles can clearly produce the basic characteristic shape of the observed ionospheric bending reasonably well. The fall in electron density below the peak value produces a positive (L2-L1) bending angle difference ($dn_e/dr > 0$). The fall in electron density above the peak produces a negative signal ($dn_e/dr < 0$). Although the vertical interval shown in Figure 3.3 is from 100 km to 800 km, it should be recalled that the l layer retrieval only assimilates bending angle in the interval from 200 km to 500 km, and the 2 layer retrieval from 120 km to 500 km. The simulated bending angles outside of these intervals are extrapolations based on the 1D-Var solution vectors, $H(\mathbf{x_a})$. It is not surprising that the fit to the observations is best in the intervals where the bending angles are used in the 1D-Var. The 1 layer solution does not fit the bending angles below 200 km very well, where the bending angles are too big. This problem seems common to most 1 layer cases. However, it does give a reasonable fit to the observations above 500 km. The two layer retrieval is clearly better than the 1 layer retrieval below 200 km, as expected. The 1 layer and 2 layer calculations are consistent with each other above 500 km, but the bending angles in both cases tend to fall too quickly when compared to this observation.

The corresponding electron density retrievals are shown in the lower panel of Figure 3.3. The 1D-Var results are the VaryChap electron density profiles computed from $\mathbf{x_a}$. By construction the 1D-Var solutions are smooth and the technique attempts to filter out the measurement noise. The 1D-Var is also unlikely to produce negative electron density values, unless the sign of the bending angle differences is wrong. The agreement between the retrieval methods near the peak electron density is encouraging. The 1 layer calculation has a much sharper fall off below the peak, but this is consistent with the larger bending angles shown in Figure 3.3. The 2 layer calculation agrees better with the Abel and AVHIRO retrievals below 200 km as expected, but it cannot produce the structure around 100 km. This structure is out outside the range used in the 1D-Var (120 km to 500 km). The AVHIRO retrieval uses all of the data in the vertical interval and can reproduce the structure near 100 km. It is interesting to note that we can reintroduce the structure to the 1D-Var solution, by exploiting

the linearity of the Abel transform and using bending angle residuals. Assuming the 1D-Var solution produces a vector of electron density values on impact parameter values, $\mathbf{n_{e,a}}$, and that the Abel transform can be written as a matrix, $\mathbf{A}$, we can write a hybrid solution using the bending angle residuals,

$$\mathbf{n_{e,h}} = \mathbf{n_{e,a}} + \mathbf{A}(\alpha_\mathbf{o} - \alpha_\mathbf{a}) \tag{3.1}$$

where $\alpha_\mathbf{o}$ and $\alpha_\mathbf{a}$ are the vector of observed and 1D-Var solution bending angle values, respectively. Note that $\alpha_\mathbf{a}$ includes all bending angles below 500 km, even if they are not used in the 1D-Var calculation, so the bending angle residuals used in Eq. 3.1 go below 120 km. In Figure 3.4 we show the impact of this "correction" on the 2 layer solution and demonstrate that the fine structure near 100 km in the Abel and AVHIRO retrievals can be reintroduced. However, whether this step is useful or necessary requires further evaluation. It is not included as an option in the ROPP 11 release.

Above 500 km, the AVHIRO approach is more consistent with the Abel solution up to 700 km in this case, and the 1D-Var estimates are lower than the Abel solution.

In the second case, shown in Figure 3.5, the 1D-Var solutions converge but to a high value. The 1D-Var solutions cannot reproduce the observed bending near 300 km, although the 2 layer retrieval is better than the 1 layer. This results in a peak electron density which is too low, when compared with the Abel transform solution. This is obviously not ideal, but it does emphasise the value of the cost at convergence ($2J/m$) diagnostic, where a scalar QC value can help identify potentially problematic retrievals. Figure 3.5 also illustrates a discontinuity in the AVHIRO retrievals near 380 km. This is common to all 143 AVHIRO retrievals, but most evident for low electron density cases, and a correction to the retrieval method is currently being developed. In this case, the 1D-Var solutions and AVHIRO electron density retrieval are either side of the Abel retrieval, and it is difficult to identify the better solution. The hybrid approach produces negative electron density values below 100 km.

Case 3 does not converge in 45 iterations in the 1 layer retrieval, but the $2J/m < 5$ (Figure 3.6). The 2 layer calculation differs slightly with convergence in 43 iterations and $2J/m = 5.2$. The 1 layer retrieval at the peak (negative) bending near 250 km appears to be slightly better than the 2 layer case. The bending above 500 km falls off too quickly, and the electron density above 500 km is lower than the Abel retrieval. Both the Abel and AVHIRO solutions have significant electron density values below 100 km, but it is questionable if these are physically realistic. The AVHIRO discontinuity at 380 km is again apparent.

Case 4 (Figure 3.7) does not converge and the $2J/m > 5$ in both the 1 layer and 2 layer retrievals, although the 2 layer retrieval is clearly a better fit to the observations. The simulated bending angle profiles struggle to capture the large bending near 300 km. However, the 2 layer electron density reproduces the Abel transform solution reasonably well. One feature that stands out from all four cases is that the height of the peak electron density appears to be very consistent between the retrieval methods.

Using bending angles above 500 km

The truncation of the measurement at 500 km will result in the loss of some ionospheric information, because the extrapolation based on the VaryChap layers will not be perfect. We can demonstrate this comparing the 1D-Var solutions when the observation vector is truncated at 500 km and truncated at 750 km. Figure 3.8 show the 2 layer 1D-Var solutions when the bending angles are assimilated up to 500 km and 750 km for the "good case" shown in Figure 3.3. Extending up to 750 km slightly improves the fit to the observed bending angles above 500 km, but there is a small degradation in the intervals between 260-280 km and $\sim$ 320-500 km. This is illustrated more clearly in Figure 3.9, which shows the (1D-Var solution - observed) bending angle differences. This could suggest that the shape of the observed bending angle profile over the 120 km to 750 km interval is difficult to produce with

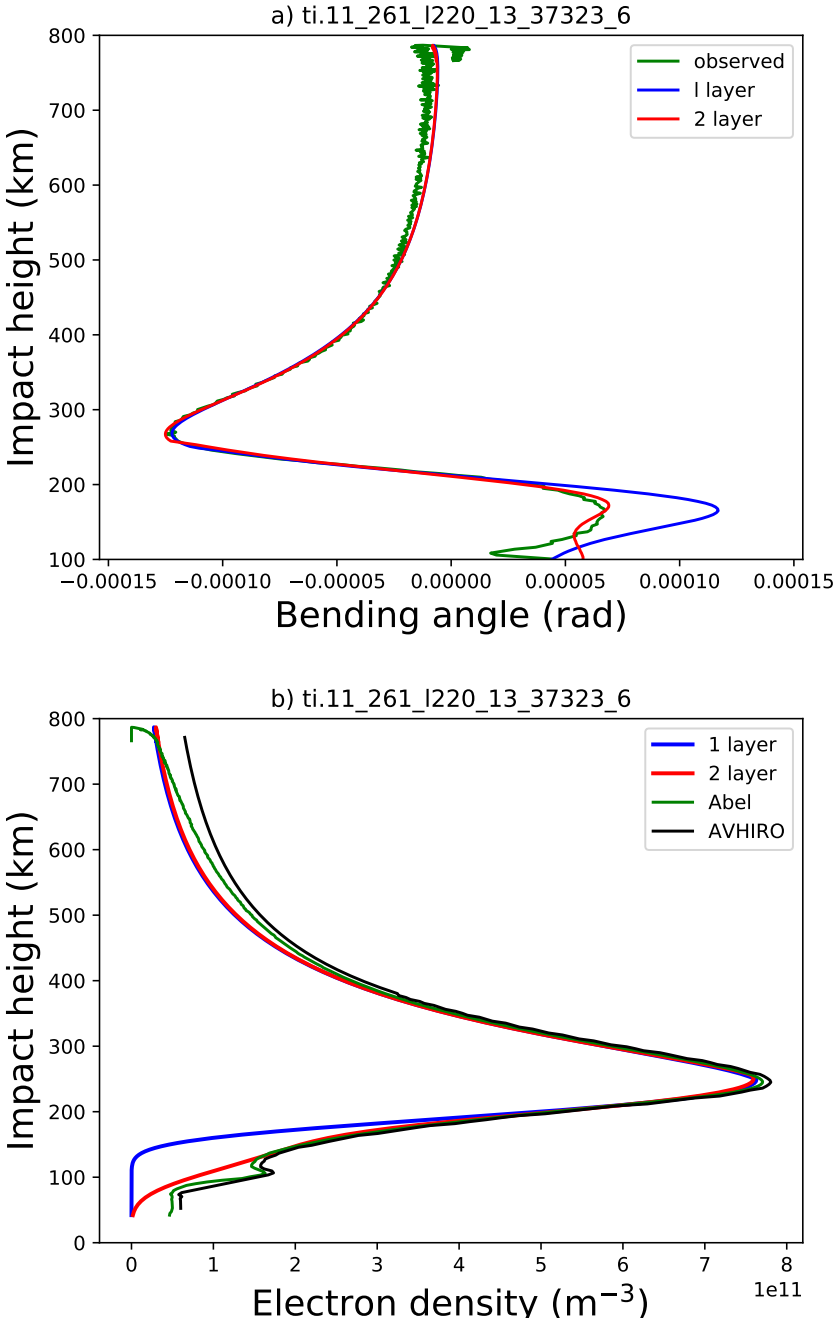

Figure 3.3: a) The bending angle profile derived from a COSMIC observation (green line) and simulated using the 1 layer (blue line) and 2 layer (red line) 1D-Var solutions. This case converges and has a reasonable $2J/m$ value. b) The electron density profiles with AVHIRO (black line). The titles are the file identifiers used in the IEEC dataset.

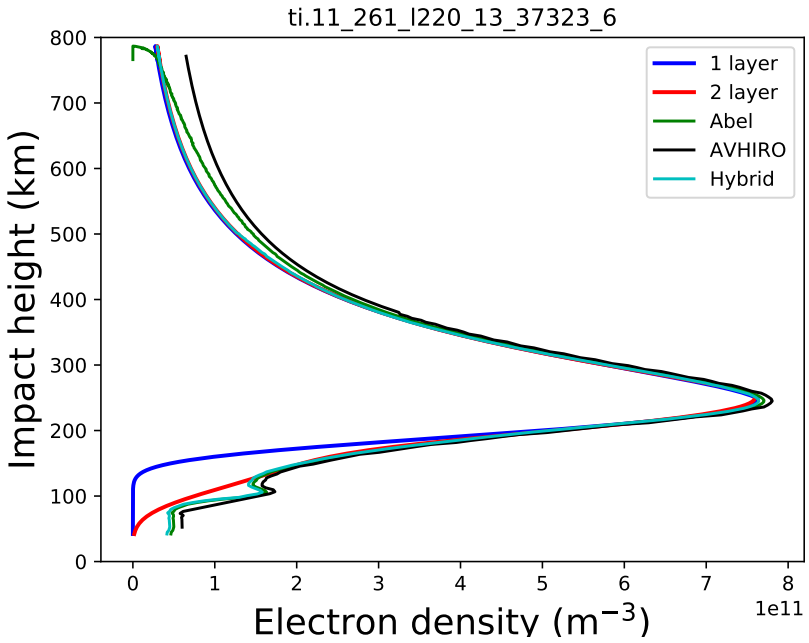

Figure 3.4: The electron density profiles for case 1, but now including the "correction" given in Eq. 3.1 to the two layer 1D-Var solution (cyan line).

the VaryChap functions, although this model clearly reproduces the main features of the ionospheric bending angle curve. Nevertheless, extending the observation to 750 km improves the consistency with the Abel electron density retrieval above 500 km.

More generally, there is some evidence from other profiles that the 500 km limit and extrapolation with the VaryChap model tends to bias the magnitude of the topside bending angles low, by around 5-10 microradians in the cases investigated here. The mean of the retrieved k values over the 143 profiles is 0.1 for the 500 km limit, but it is 0.18 for the 750 km limit (The latter might be a better value for the k *a priori* estimate in Table 3.1.). However, this area is investigated in more detail in the VS39. Extrapolation with a Chapman model does not improve this (Figure not shown).

Role of the *a priori* information

In general, the 1D-Var approach uses *a priori* information to help constrain the solution of ill-posed problems, where multiple estimates of the state, $\mathbf{x}$, can produce the same observation values, $\mathbf{y}$. An example of an ill-posed problem is the tropospheric water vapour ambiguity problem in neutral atmosphere GNSS-RO applications (Healy and Eyre, 2000; Palmer *et al*. 2000). However, the truncated ionospheric retrieval problem appears to be well-posed. The bending angles in the vertical interval from 120 km to 500 km can constrain the seven parameters (Seven, because the k for the lower layer is fixed.) that determine the two layers. The prior information, $\mathbf{x_b}$, is effectively a starting point for the minimisation process, rather than being a strong constraint on the final 1D-Var solution. Figure 3.10 shows observed bending angle profile (green line) and both the $H(\mathbf{x_b})$ and $H(\mathbf{x_a})$ for the bending angles used in the 2 layer 1D-Var solution. This illustrates how far the solution moves away from the background in bending angle space in order to fit the observations to within their assumed errors. In addition, the diagonal elements of the theoretical solution error covariance matrix, $\mathbf{A}$ (Eq. 2.2), are significantly smaller than the diagonal elements of $\mathbf{B}$, again indicating that this retrieval problem is

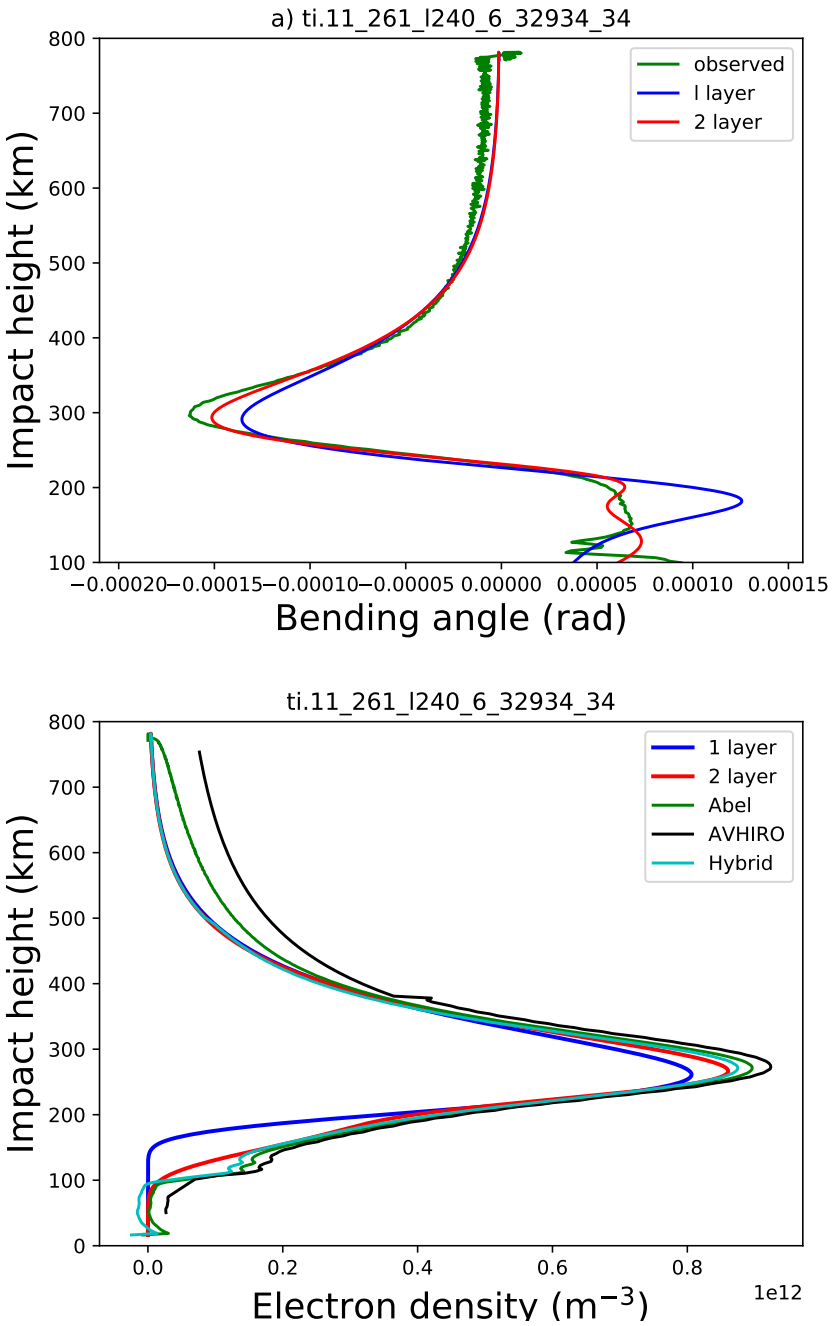

Figure 3.5: a) The bending angle profile derived from a COSMIC observation (green line) and simulated using the 1 layer (blue line) and 2 layer (red line) 1D-Var solutions. This cases converges but $2J/m > 5$. b) The electron density profiles with AVHIRO (black line) and the hybrid solution (cyan).

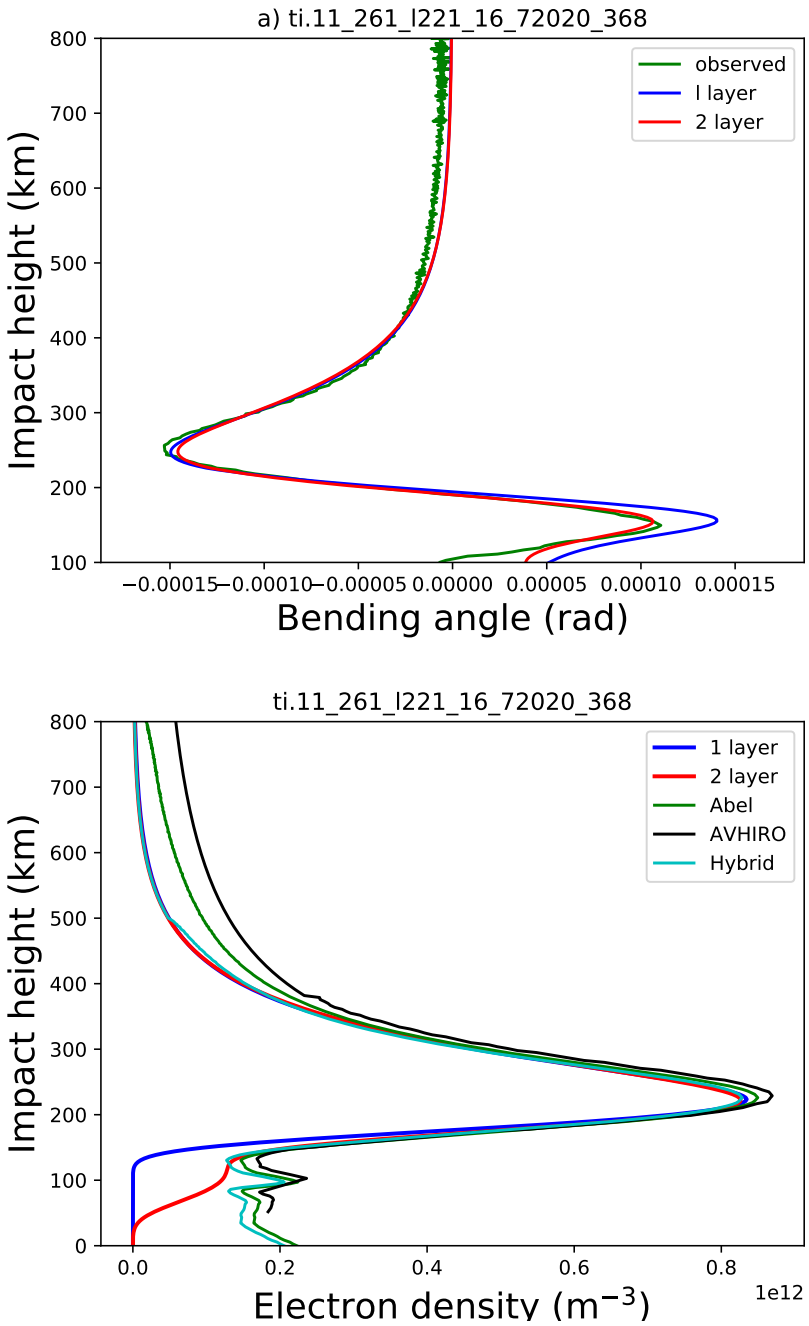

Figure 3.6: a) The bending angle profile derived from a COSMIC observation (green line) and simulated using the 1 layer (blue line) and 2 layer (red line) 1D-Var solutions. This case does not converge but $2J/m < 5$. b) The electron density profiles with AVHIRO (black line) and the hybrid solution (cyan).

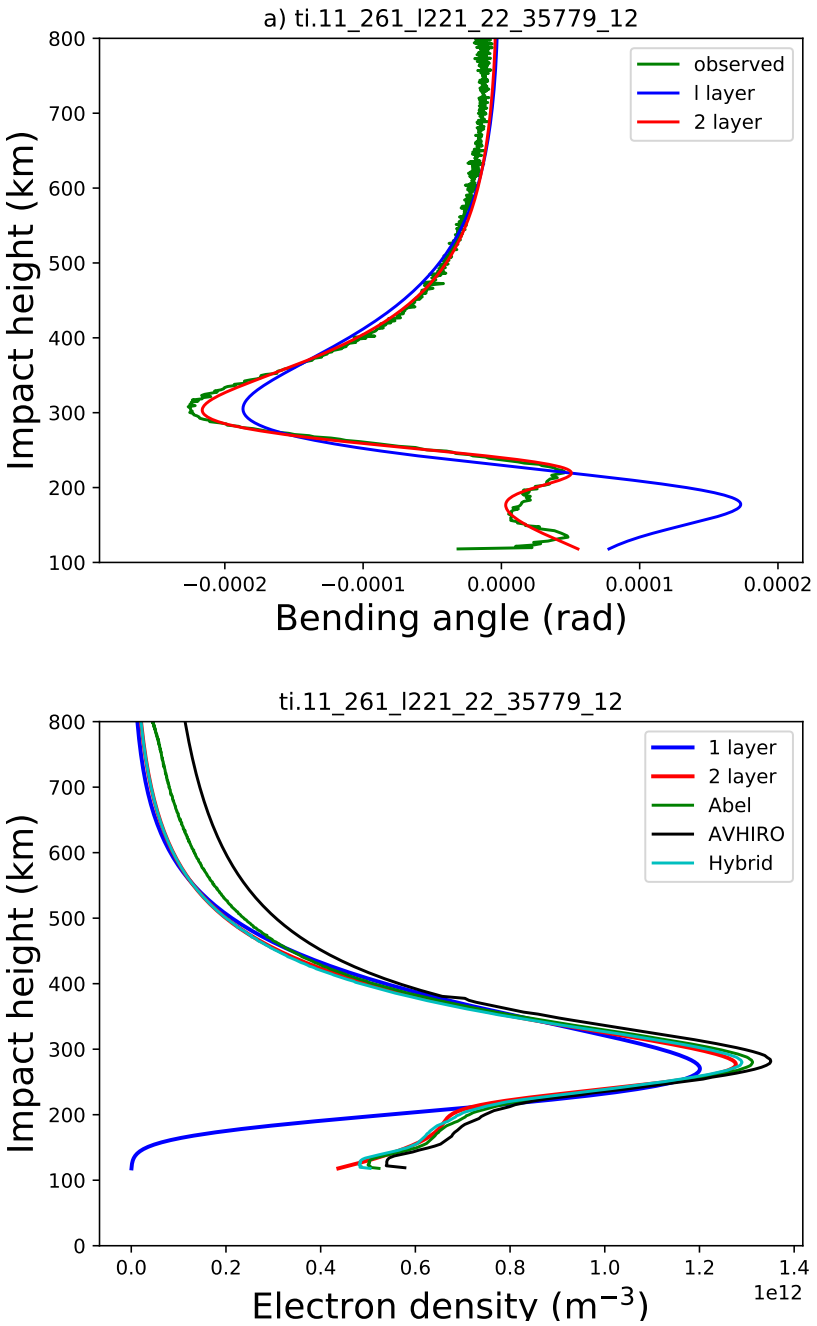

Figure 3.7: a) The bending angle profile derived from a COSMIC observation (green line) and simulated using the 1 layer (blue line) and 2 layer (red line) 1D-Var solutions. This case does not converge and $2J/m > 5$ in both the 1 layer and 2 layer retrievals. b) The electron density profiles with AVHIRO (black line) and the hybrid solution (cyan).

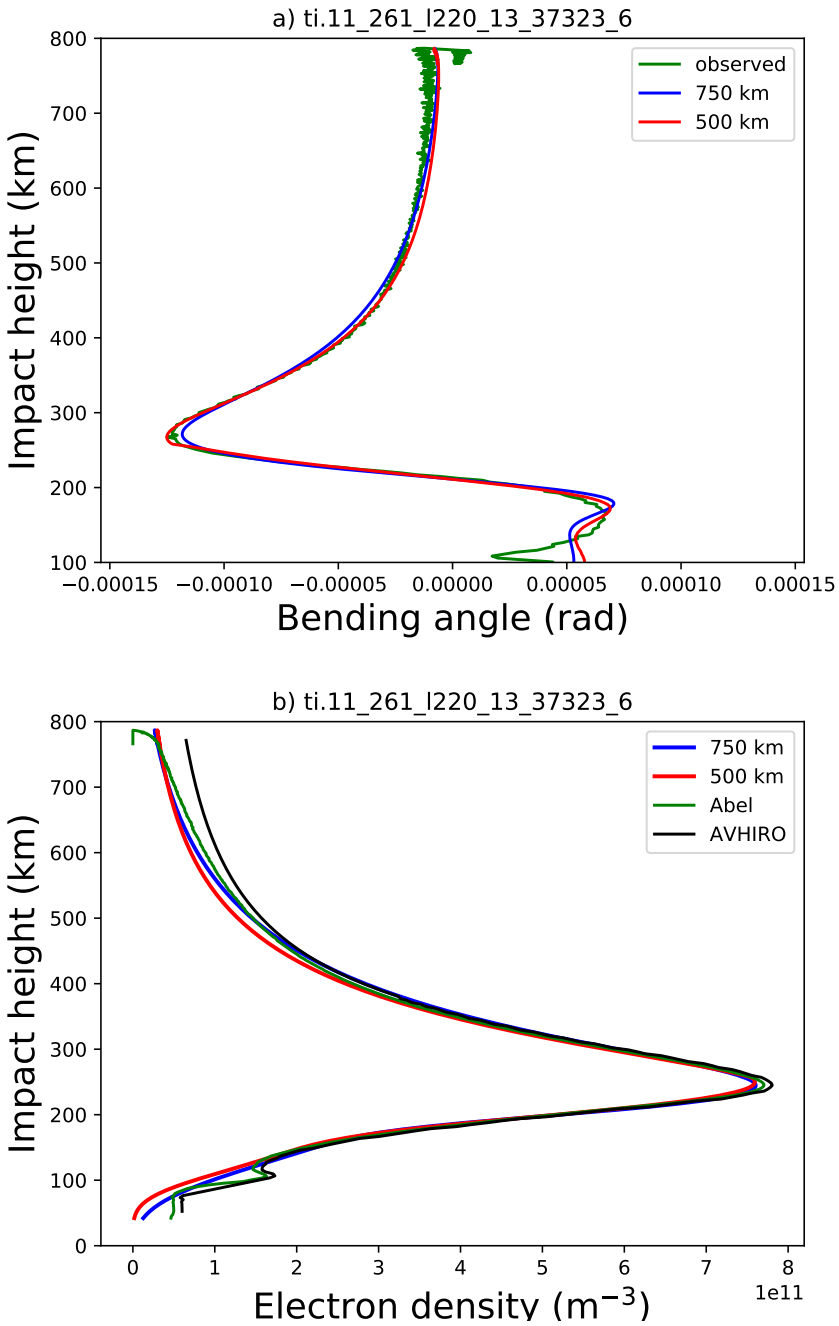

Figure 3.8: a) The bending angle profile derived from a COSMIC observation (green line) and simulated using the 2 layer 1D-Var solution with bending angles up to 500 km (red line) and 750 km (black line). This case does not converge and $2J/m > 5$ in both the 1 layer and 2 layer retrievals. b) The electron density profiles with AVHIRO (black line).

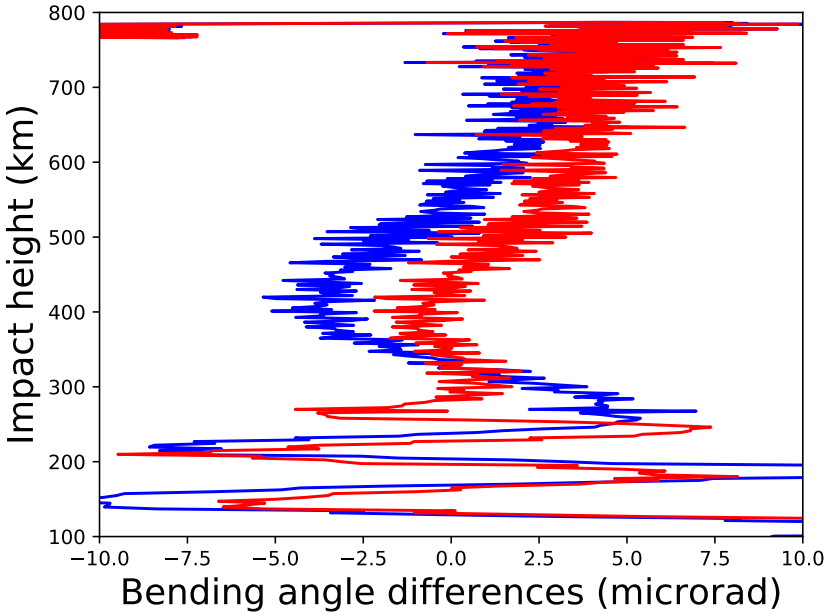

Figure 3.9: The bending angle (1D-Var minus observed) bending angle differences for case 1 for the 750 km (blue line) and 500 km (red line) 1D-Var solutions.

well-posed. The background and analysis uncertainty estimates – given by the square-root of the diagonals of the $\mathbf{B}$ and $\mathbf{A}$, respectively – are shown in Table 3.2 for the 2 layer retrieval of case 1. As noted above, the k of the lower layer is fixed in these retrievals, so by construction the bending angles cannot improve the estimate of it.

Table 3.2: The background and analysis uncertainty estimates for case 1, using the 2 layer retrieval with bending angles up to 500 km.

Layer number	Variable	Background σ_b	Analysis σ_a	σ_a/σ_b
1	n_m (m^{-3})	5.0e11	1.4e10	0.028
1	$r_m - R_c$ (m)	1.5e5	5.5e2	0.004
1	H_m(m)	2.5e4	5.7e2	0.023
1	k (m/m)	0.075	0.014	0.186
2	n_m (m^{-3})	2.5e10	7.9e9	0.316
2	$r_m - R_c$(m)	2.0e4	4.2e3	0.211
2	H_m(m)	1.0e4	2.18e3	0.218
2	k (m/m)	7.5e-6	7.5e-6	1.0

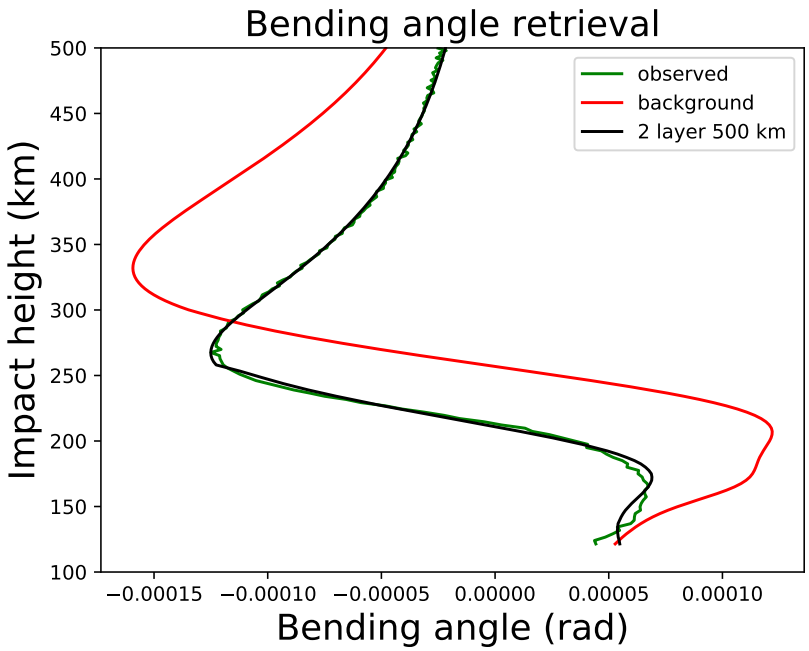

Figure 3.10: The observed (green line), background (red line) and 1D-Var solution (black line) bending angle profiles for "case 1", for a 2 layer retrieval using bending angles in the vertical interval from 120 km to 500 km.

4 Discussion and Conclusions

The aim of this work has been to develop a 1D-Var ionospheric retrieval that can be applied to the Metop-SG measurement geometry, which will truncate the ionospheric GNSS-RO measurements around 500 km above the surface. This is a new, general approach for the ionospheric GNSS-RO retrieval problem which should be valid for both the truncated and standard GNSS-RO measurement geometry. The original plan was to assimilate L1-L2 slant TEC differences as a function of impact parameter in the 1D-Var, but we have used L2-L1 bending angle differences. This approach is closer to how GNSS-RO data is used in neutral atmosphere applications, such as operational NWP.

A new 1D ionospheric bending angle forward operator has been developed that computes L2-L1 bending angle differences as a function of impact parameter, assuming that the ionospheric electron density can be modeled with multiple VaryChap layers. The L2-L1 bending angle uncertainty is assumed to be 2 microradians, and vertical error correlations are neglected.

Firstly, gradient based minimisation techniques can be successfully applied to this retrieval problem, and the non-linearity of the VaryChap functions is not problematic. Only 8 of the 143 cases investigated fail to converge in 45 iterations. Some cases converge to a high cost function value, but this is useful QC information and it could be used to identify problematic retrievals in any future operational system. More precisely, 25 and 21 cases converge to $2J/m > 5$ in the 1 layer and 2 layer retrievals, respectively.

The 1D-Var tries to filter out measurement noise and the 1D-Var retrieved electron density solutions are smooth in comparison with the Abel transform retrieval. Fine structure below 500 km can be introduced with an additional processing step (Eq. 3.1) if required. It is highly unlikely for the 1D-Var to produce unphysical negative electron density values. There are no negative electron density values in the 143 cases we considered here. Two layer retrievals are better than a single layer, because the electron density falls too quickly below the peak value when only 1 layer is used. The 2 layer retrieval problem is well-posed when bending angles in the 120 km to 500 km vertical interval are available. This means that the truncated data should be useful for ionospheric data assimilation applications, and provide useful information. The *a priori* information is essentially a first guess used to start the minimisation, rather than a strong constraint on the final 1D-Var solution. Better *a priori* information might speed up convergence but not necessarily improve the 1D-Var solution. However, better *a priori* would also be useful for QC, because it would be easier to screen out poor bending angle values at the start of the 1D-Var.

There is one issue with the approach that requires further consideration. Truncating the bending angles at 500 km cannot produce an electron density estimate as accurate as when the measurements are available to the height of the LEO satellite. The VaryChap retrieval with an upper limit of 500 km may produce extrapolated (negative) bending angles above 500 km that fall off too quickly, and which are too small (see Figure 3.9). This has been investigated in more detail in VS39, but it may also need to be investigated in future work. In particular, testing other formulations of the electron density profile used in the 1D-Var might be helpful.

Finally, the use of bending angles may have implications for how GNSS-RO data is used in ionospheric data assimilation (DA) systems. In general, slant TEC values are assimilated in ionospheric DA systems, but these require a correction for the Differential Code Biases (DCB). If the DCB bias is constant during the occultation, it will not impact the bending angle values derived from the raw phase delays, and so it is not required to assimilate these measurements. This should be investigated.

Table 4.1: The IEEC data files.

Case number	IEEC Identifier
1	ti.11_261_l220_13_37323_6
2	ti.11_261_l240_6_32934_34
3	ti.11_261_l221_16_72020_368
4	ti.11_261_l221_22_35779_12

Acknowledgments

We thank Dr Haixia Lyu and Dr Hernández-Pajares for providing the COSMIC data used here, and the AVHIRO retrieval results. Dr Stig Syndergaard drew our attention to the Abel transform retrieval problems associated with the singularity at $r = r_L$. Dr Sean Elvidge is thanked for sharing VS39 results and useful discussions throughout the work. Dr Riccardo Notarpietro is thanked for useful discussions during the early stages of this work.

Appendix A: Four IEEC cases shown

The test data was provided by IEEC, Barcelona, Spain and they can be made available on request. The four cases used in section 3 are shown in Table 4.1.

The "ti" filename convention (e.g. ti.11_261_l220_13_37323_6) can be decomposed as follows (Dr Hernández-Pajares, pers. comm):

- 11 = year =2011
- 261 = day of year
- l220 = receiver identifier.
- 13 = GPS PRN identifier.
- 37323 = Approximate starting GPS time in seconds of day
- 6 = transmitter-receiver phase-continuous-arc number

Appendix B: Abel Transform Retrievals

Schreiner *et al.* (1999) provide two versions of the Abel transform inversion, one based on the derivative of STEC, dS/da, and the other using bending angle. One interesting aspect of the Abel transform pairs is that bending angle formulation has an explicit dependence on the refractive index at the LEO satellite, $n(r_L)$, but the phase derivative form does not appear to. However, the phase derivative form relies on the singularity of dS/da at $r = r_L$ which is not measurable. Lei *et al.* (2007) discuss the retrieval difficulties associated with the singularity of the phase derivative at $r = r_L$. In practice, the Abel transform using dS/da also requires $n_e(r_L)$ information from another source or a modified retrieval approach.

We can compare the two Abel transforms, and demonstrate how they are related. If the STEC derivatives can be “corrected” – or calibrated – to only include the phase delay, S^p, associated with

just the "partial" section of ray path where $r \leq r_L$ we can write,

$$\frac{dS^p}{da} = -\frac{2n_e(r_L)a}{\sqrt{(r_L^2 - a^2)}} + 2a\int_a^{r_L} \frac{\frac{dn_e(r)}{dr}}{\sqrt{(r^2 - a^2)}} dr \tag{4.1}$$

This can be inverted with an Abel transform (Eq. 14, Schreiner *et al.* 1999)

$$n_e(r) = -\frac{1}{\pi}\int_r^{r_L} \frac{\frac{dS^p}{da}}{\sqrt{(a^2 - r^2)}} da. \tag{4.2}$$

Inserting Eq. 4.1 into Eq. 4.2, and noting that *for all* $r \leq r_L$,

$$\int_r^{r_L} \frac{2n_e(r_L)a}{\sqrt{(a^2 - r^2)(r_L^2 - a^2)}} da = n_e(r_L)\pi \tag{4.3}$$

the Abel transform can be written as

$$n_e(r) = n_e(r_L) - \frac{f_i^2}{\pi k_4}\int_r^{r_L} \frac{\alpha_i^p}{\sqrt{(a^2 - r^2)}} da \tag{4.4}$$

where f_i is the signal frequency, and the "partial" bending angle, for the section of path where $r \leq r_L$, is approximately

$$\alpha_i^p = \frac{2ak_4}{f_i^2}\int_a^{r_L} \frac{\frac{dn_e}{dr}}{\sqrt{r^2 - a^2}} dr. \tag{4.5}$$

The Abel transform pair using bending angles is (Eq. 8,9, Schreiner *et al.* 1999),

$$\begin{aligned} \alpha_i^p(a) &= -2a\int_a^{x_L} \frac{\frac{d\ln n}{dx}}{\sqrt{x^2 - a^2}} dx \\ n(x) &= n(r_L)\exp\left(\frac{1}{\pi}\int_x^{x_L} \frac{\alpha_i^p}{\sqrt{a^2 - x^2}} da\right) \end{aligned} \tag{4.6}$$

where the refractive index $n = 1 - k_4 n_e / f_i^2$, and $x = nr$. In the ionosphere, all refractive index values are close to unity, and the bending angles are small. For example, assuming a high electron of $3 \times 10^{12}\mathrm{m}^{-3}$, most appropriate for daytime, solar maximum conditions, and assuming a signal frequency $f_2 = 1227.60$ MHz, then $k_4 n_e / f_2^2 = 8 \times 10^{-5}$ (or 80 refractivity units). In this case, $|x - r| = 8 \times 10^{-5} r <$ 600m.

So in the bending angle integral we can assume $x \simeq r$, expand $\frac{d\ln n}{dx} \simeq -(k_4/f_i^2) dn_e/dr$, and recover Eq. 4.5. We can also expand the exponential in Eq. 4.6 with $\exp(u) \simeq 1 + u$. These simplifications lead to,

$$\begin{aligned} 1 - \frac{k_4}{f_i^2} n_e(r) &\simeq \left(1 - \frac{k_4}{f_i^2} n_e(r_L)\right)\left(1 + \frac{1}{\pi}\int_r^{r_L} \frac{\alpha_i^p}{\sqrt{a^2 - r^2}} da\right) \\ &\simeq 1 - \frac{k_4}{f_i^2} n_e(r_L) + \frac{1}{\pi}\int_r^{r_L} \frac{\alpha_i^p}{\sqrt{a^2 - r^2}} da + \ldots O(n_e^2) \end{aligned} \tag{4.7}$$

and we recover the phase derivative formulation given in Eq. 4.4.

References

Dyrud, L., A. Jovancevic, A. Brown, D. Wilson, and S. Ganguly, 2008: Ionospheric measurement with GPS: Receiver techniques and methods. *Radio Science*, **43**, 6, doi.org/10.1029/2007RS003770.

Elvidge, S., 2021: Ionospheric 1D-Var Retrieval Assessment. *ROM SAF Visiting Scientist Report*, **39**, https://www.romsaf.org/Publications/reports/.

Hajj, G. A., and L. J. Romans, 1998: Ionospheric electron density profiles obtained with the Global Positioning System: Results from the GPS/MET experiment. *Radio Sci.*, **33**, 175–190.

Healy, S. B., and J. R. Eyre, 2000: Retrieving temperature, water vapor and surface pressure information from refractive–index profiles derived by radio occultation: A simulation study. *Q. J. R. Meteorol. Soc.*, **126**, 1661–1683.

Jensen, A., M. Lohmann, H.-H. Benzon, and A. Nielsen, 2003: Full Spectrum Inversion of radio occultation signals. *Radio Sci.*, **38**, 1040, doi:10.1029/2002RS002763.

Kursinski, E. R., G. A. Hajj, J. T. Schofield, R. P. Linfield, and K. R. Hardy, 1997: Observing earth's atmosphere with radio occultation measurements using the Global Positioning System. *J. Geophys. Res.*, **102**, 23.429–23.465.

Lei, J., S. Syndergaard, A. G. Burns, S. C. Solomon, W. Wang, Z. Zeng, R. G. Roble, Q. Wu, Y.-H. Kuo, J. M. Holt, S.-R. Zhang, D. L. Hysell, F. S. Rodrigues, and C. H. Lin, 2007: Comparison of COSMIC ionospheric measurements with ground-based observations and model predictions: Preliminary results. *JGR: Space Physics*, **112**, A7, doi.org/10.1029/2006JA012240.

Lyu, H., M. Hernández-Pajares, E. Monte-Moreno, and E. Cardellach, 2019: Electron Density Retrieval From Truncated Radio Occultation GNSS data. *JGR: Space Physics*, **124**, 6, 4842–4851.

Nsumei, P., B. W. Reinisch, X. Huang, and D. Bilitza, 2012: New Vary-Chap profile of the topside ionosphere electron density distribution for use with the IRI model and the GIRO real time data. *Radio Science*, **47**, 4, doi.org/10.1029/2012RS004989.

Palmer, P. I., J. J. Barnett, J. R. Eyre, and S. B. Healy, 2000: A nonlinear optimal estimation inverse method for radio occultation measurements of temperature, humidity, and surface pressure. *J. Geophys. Res.*, **105**, 17.513–17.526.

Poli, P., S. B. Healy, and D. P. Dee, 2010: Assimilation of Global Positioning System radio occultation data in the ECMWF ERA-Interim reanalysis. *Q. J. R. Meteorol. Soc.*, **136**, 1972–1990.

Press, W., S. Teukolsky, W. Vetterling, and B. Flannery, 1992: *Numerical recipes in Fortran – The art of scientific computing*, 2nd ed. Cambridge University Press, Cambridge, New York.

Rodgers, C. D., 2000: *Inverse methods for atmospheric sounding: Theory and practice*. World Scientific Publishing, Singapore, New Jersey, London, Hong Kong.

Schreiner, W. S., S. V. Sokolovskiy, C. Rocken, and D. C. Hunt, 1999: Analysis and validation of GPS/MET radio occultation data in the ionosphere. *Radio Sci*, **34**, 949–966.

Vorob'ev, V. V., and T. G. Krasil'nikova, 1994: Estimation of the accuracy of the atmospheric refractive index recovery from doppler shift measurements at frequencies used in the NAVSTAR system. *USSR Phys. Atmos. Ocean, Engl. Transl.*, **29**, 602–609.

ROM SAF (and earlier GRAS SAF) Reports

SAF/GRAS/METO/REP/GSR/001	Mono-dimensional thinning for GPS Radio Occulation
SAF/GRAS/METO/REP/GSR/002	Geodesy calculations in ROPP
SAF/GRAS/METO/REP/GSR/003	ROPP minimiser - minROPP
SAF/GRAS/METO/REP/GSR/004	Error function calculation in ROPP
SAF/GRAS/METO/REP/GSR/005	Refractivity calculations in ROPP
SAF/GRAS/METO/REP/GSR/006	Levenberg-Marquardt minimisation in ROPP
SAF/GRAS/METO/REP/GSR/007	Abel integral calculations in ROPP
SAF/GRAS/METO/REP/GSR/008	ROPP thinner algorithm
SAF/GRAS/METO/REP/GSR/009	Refractivity coefficients used in the assimilation of GPS radio occultation measurements
SAF/GRAS/METO/REP/GSR/010	Latitudinal Binning and Area-Weighted Averaging of Irregularly Distributed Radio Occultation Data
SAF/GRAS/METO/REP/GSR/011	ROPP 1dVar validation
SAF/GRAS/METO/REP/GSR/012	Assimilation of Global Positioning System Radio Occultation Data in the ECMWF ERA-Interim Re-analysis
SAF/GRAS/METO/REP/GSR/013	ROPP PP validation
SAF/ROM/METO/REP/RSR/014	A review of the geodesy calculations in ROPP
SAF/ROM/METO/REP/RSR/015	Improvements to the ROPP refractivity and bending angle operators
SAF/ROM/METO/REP/RSR/016	Simplifying EGM96 undulation calculations in ROPP
SAF/ROM/METO/REP/RSR/017	Simulation of L1 and L2 bending angles with a model ionosphere
SAF/ROM/METO/REP/RSR/018	Single Frequency Radio Occultation Retrievals: Impact on Numerical Weather Prediction
SAF/ROM/METO/REP/RSR/019	Implementation of the ROPP two-dimensional bending angle observation operator in an NWP system
SAF/ROM/METO/REP/RSR/020	Interpolation artefact in ECMWF monthly standard deviation plots
SAF/ROM/METO/REP/RSR/021	5th ROM SAF User Workshop on Applications of GPS radio occultation measurements
SAF/ROM/METO/REP/RSR/022	The use of the GPS radio occultation reflection flag for NWP applications
SAF/ROM/METO/REP/RSR/023	Assessment of a potential reflection flag product
SAF/ROM/METO/REP/RSR/024	The calculation of planetary boundary layer heights in ROPP
SAF/ROM/METO/REP/RSR/025	Survey on user requirements for potential ionospheric products from EPS-SG radio occultation measurements

ROM SAF (and earlier GRAS SAF) Reports (cont.)

SAF/ROM/METO/REP/RSR/026	Estimates of GNSS radio occultation bending angle and refractivity error statistics
SAF/ROM/METO/REP/RSR/027	Recent forecast impact experiments with GPS radio occultation measurements
SAF/ROM/METO/REP/RSR/028	Description of wave optics modelling in ROPP-9 and suggested improvements for ROPP-9.1
SAF/ROM/METO/REP/RSR/029	Testing reprocessed GPS radio occultation datasets in a reanalysis system
SAF/ROM/METO/REP/RSR/030	A first look at the feasibility of assimilating single and dual frequency bending angles
SAF/ROM/METO/REP/RSR/031	Sensitivity of some RO measurements to the shape of the ionospheric electron density profile
SAF/ROM/METO/REP/RSR/032	An initial assessment of the quality of RO data from KOMPSAT-5
SAF/ROM/METO/REP/RSR/033	Some science changes in ROPP-9.1
SAF/ROM/METO/REP/RSR/034	An initial assessment of the quality of RO data from Metop-C
SAF/ROM/METO/REP/RSR/035	An initial assessment of the quality of RO data from FY-3D
SAF/ROM/METO/REP/RSR/036	An initial assessment of the quality of RO data from PAZ
SAF/ROM/METO/REP/RSR/037	6th ROM SAF User Workshop
SAF/ROM/METO/REP/RSR/038	An initial assessment of the quality of RO data from COSMIC-2
SAF/ROM/METO/REP/RSR/039	Impacts of RO mission differences on trends in multi-mission data records
SAF/ROM/METO/REP/RSR/040	Anomalous GRAS radio occultations
SAF/ROM/METO/REP/RSR/041	Assessment of sensitivity of the ROM SAF 1D-Var solutions to various error covariance choices

ROM SAF Reports are accessible via the ROM SAF website: http://www.romsaf.org